

Optics Letters

Silicon-based on-chip electrically tunable sidewall Bragg grating Fabry–Perot filter

WEIFENG ZHANG, NASRIN EHTESHAMI, WEILIN LIU, AND JIANPING YAO*

Microwave Photonic Research Laboratory, School of Electrical Engineering and Computer Science, University of Ottawa, 800 King Edward Avenue, Ottawa, Ontario K1N 6N5, Canada

*Corresponding author: jpyao@eecs.uottawa.ca

Received 15 April 2015; accepted 10 June 2015; posted 12 June 2015 (Doc. ID 238156); published 29 June 2015

We report the design, fabrication, and testing of a silicon-based on-chip electrically tunable sidewall Bragg grating Fabry–Perot filter. Spectral measurement shows that the filter has a narrow notch in reflection of approximately 46 pm, a Q-factor of 33,500, and an extinction ratio of 16.4 dB. DC measurement shows that the average central wavelength shift rates with forward and reverse bias are -1.15 nm/V and 4.2 pm/V, respectively. Due to strong light confinement in the Fabry–Perot cavity, the electro-optic frequency response shows that the filter has a 3-dB modulation bandwidth of ~5.6 GHz. The performance of using the filter to perform modulation of a 3.5 Gb/s $2^7 - 1$ nonreturn-to-zero pseudorandom binary sequence is evaluated. © 2015 Optical Society of America

OCIS codes: (250.0250) Optoelectronics; (050.2770) Gratings; (130.3120) Integrated optics devices.

<http://dx.doi.org/10.1364/OL.40.003153>

Owing to the unique feature of a narrow transmission window within its stopband, a Bragg grating Fabry–Perot filter (BG-FPF) [1,2] has been considered a key photonic component that can find numerous applications such as narrowband filtering [3], optical sensing [4], and optical signal processing [5]. In addition, a BG-FPF with an ultra-narrow transmission window can also be used in a photonic subsystem for mode selection. For example, a BG-FPF can be incorporated in a laser cavity to ensure narrow linewidth operation [6]. In a high-capacity optical communications system where dense wavelength division multiplexing (DWDM) is employed, accurate channelization is needed, which can be implemented using an array of BG-FPFs with precisely controlled wavelength spacing [7]. However, the optical properties of a BG-FPF are predetermined by its design, which is fixed once the device is fabricated. In addition, due to fabrication imperfections, there are always discrepancies in the optical properties of an actually fabricated BG-FPF. Therefore, the fixed optical properties and the unavoidable fabrication discrepancies may limit BG-FPFs for wide applications. Furthermore, for an adaptive sensor system and a

reconfigurable optical communication network, a frequency-tunable transmission filter is always required [8]. A frequency-tunable BG-FPF is a candidate for such applications.

In this Letter, we propose for the first time to the best of our knowledge, a silicon-based on-chip electrically tunable sidewall Bragg grating Fabry–Perot filter (TBG-FPF). The TBG-FPF consists of two sidewall Bragg gratings on a rib waveguide as two reflectors, and a lateral PN junction formed in the waveguide to achieve electrical tunability. The tunability is achieved by tuning a bias voltage applied to the PN junction based on the plasma dispersion effect. The TBG-FPF is designed, fabricated, and tested. Spectral measurement shows that the linewidth of the notch in the reflection band is approximately 46 pm with a Q-factor of 33,500, and an extinction ratio is 16.4 dB. DC performance of the TBG-FPF is also evaluated. The average central wavelength shift rates for a forward and reverse bias are -1.15 nm/V and 4.2 pm/V, respectively. Since the light-confining resonating structure of the Fabry–Perot (FP) cavity can enhance the effect of refractive index change, the TBG-FPF can be employed as an electro-optic modulator. The electro-optic frequency response is measured that shows a 3-dB modulation bandwidth of ~5.6 GHz. The performance of using the filter as an electro-optic modulator to perform high-speed modulation of a 3.5 Gb/s $2^7 - 1$ nonreturn-to-zero pseudorandom binary sequence is evaluated.

Figure 1(a) illustrates the perspective view of the proposed TBG-FPF. It is fabricated on a silicon-on-insulator (SOI) substrate with a bottom silica layer of 2 μm in thickness and a top silicon layer of 220 nm in thickness. The cladding layer of silica is removed in Fig. 1(a) to clearly illustrate the internal structure of the device. The silicon rib waveguide with 500-nm in width, 220-nm in height, and 90-nm in slab thickness is employed to ensure a single fundamental TE mode operation. The inset in Fig. 1(a) shows a simulated mode profile of the fundamental TE mode at 1550 nm. To achieve a higher tuning efficiency, an asymmetrical lateral PN junction is adopted to enable electrical tuning of the grating based on the plasma dispersion effect [9]. As shown in Fig. 1(b), the PN junction is slightly shifted to the left from the center of the waveguide by 50 nm, to increase the mode overlap with the p-type doping region, since the plasma dispersion effect is more sensitive to

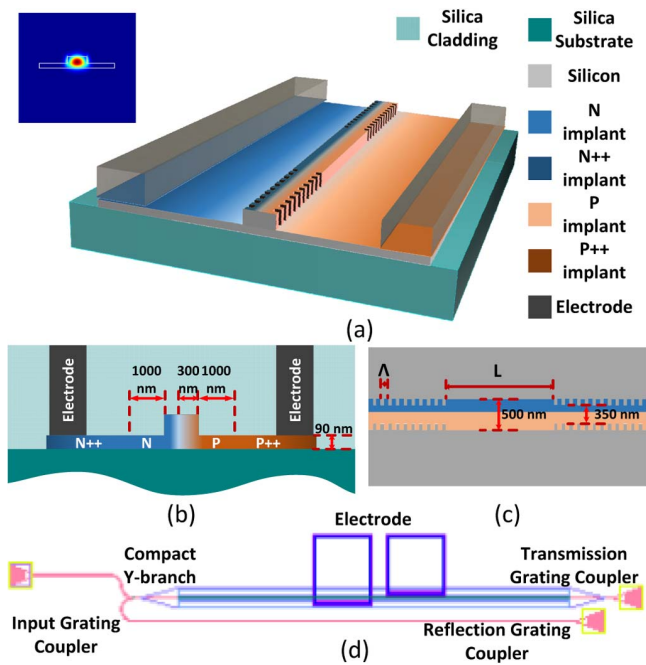


Fig. 1. (a) Perspective view of the proposed TBG-FPF (inset: simulated fundamental TE mode profile of the rib waveguide). (b) Cross-sectional view of proposed TBG-FPF. (c) Top view of the FP cavity. (d) Schematic layout of the proposed TBG-FPF.

the change of the free-hole concentration. Additional p++ and n++ implantations, 1 μm away from the rib to minimize absorption losses, are utilized for ohmic contact formation. Figure 1(c) provides the top view of the grating structure on the rib and the FP cavity. The periodic sidewall corrugations with a depth of 75 nm are introduced to the rib. The grating period Λ is 310 nm with a duty cycle of 50%, corresponding to a Bragg wavelength of 1550 nm. The total length of the grating is 1240 μm . The FP cavity, with a length L of 24.025 μm , is allocated at the center of the grating. Figure 1(d) shows the schematic layout of the device. Three TE-mode grating couplers [10] are used to couple light between the chip and the input and output fibers, and a compact Y-branch [11] is used to collect the reflected light. To minimize the chip footprint and reduce the bending loss, a strip waveguide is used to guide the light signal between the grating coupler and the filter. Since the filter is designed on a rib waveguide, a double-layer linear taper waveguide with a length of 50 μm is used for the transition between the strip and the rib waveguides. Two contact windows are opened on the silica pads, with 2- μm -thick aluminum layer deposited to make the contacts. The entire device is 1.58 mm in length and 0.130 mm in width, giving a small footprint of 0.205 mm².

The optical performance of the TBG-FPF is first evaluated. To do so, we use an optical vector analyzer (LUNA OVA CTe) to measure the reflection and transmission spectra of the fabricated TBG-FPF. Figure 2 shows the spectra when a zero bias voltage is applied. It can be seen there is a resonant window within the stopband in the transmission spectrum. The notch in the reflection band has a 3-dB bandwidth of 46 pm with a Q-factor of 33,500, and an extinction ratio of 16.4 dB. The

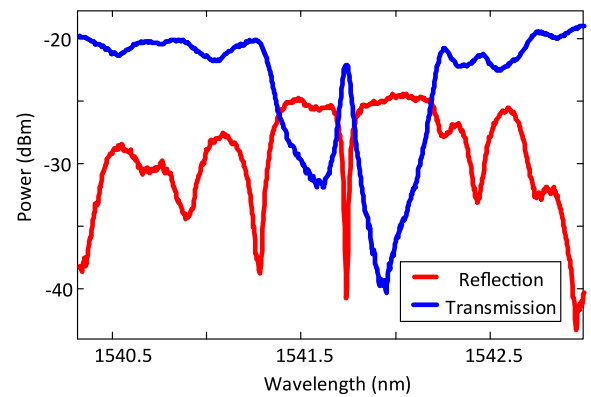


Fig. 2. Measured reflection and transmission spectra of the TBG-FPF with a zero bias voltage applied.

Bragg wavelength is shifted to 1541.75 nm due to the inevitable fabrication imperfections. Strong sidelobes in the reflection spectrum are seen, which can be suppressed by applying apodization to the grating [12]. The insertion loss of the TBG-FPF is 19 dB, which consists of the fiber-to-fiber I/O coupling loss of 15.6 dB, the grating induced loss of 2.1 dB, and the loss due to the ion implantations of about 1.3 dB. Therefore, the optical excess propagation loss caused by ion implantation is 10.3 dB/cm. Note that the fiber-to-fiber I/O coupling loss is measured using a reference rib waveguide without a grating and without ion implantation. The grating induced loss, which mainly results from the sidewall scattering, is measured using a reference sidewall grating on a rib waveguide without ion implantation.

Then, the DC performance of the TBG-FPF is evaluated for the PN junction being forward biased. Figure 3(a) shows the voltage–current (V-I) curve of the PN junction, which indicates that the junction is turned on at about -0.7 V. Figure 3(b) shows the transmission spectrum, which is blue-shifted when the bias voltage is increased. Since the current is injected uniformly along the entire length of the device, the wavelengths of the stopband and the transmission window are both shifted to shorter wavelengths. The blue shifts result from the decrease in the refractive index induced by the free-carrier injection. In addition, the injected free-carrier would also introduce an excess absorption loss, which would degrade the performance of the filter. To illustrate the performance degradation clearly, we show in detail the wavelength shift of the notch in the reflection band in Fig. 3(c). As can be seen when the bias voltage is increasing, the Q-factor and the extinction ratio of the filter are reducing. For a current of 6.070 mA when operating at -1.0 V, the Q-factor is reduced to 25,700, and the extinction ratio is reduced to 5 dB. The blue shift of the notch wavelength is found to be 0.345 nm. The tuning of the spectral response when increasing the bias voltage is shown in Fig. 3(d). The wavelength shift rate is estimated to be -1.15 nm/V after the PN junction is turned on.

The DC performance of the TBG-FPF when the PN junction is reverse biased is also evaluated. As can be seen from Fig. 4(a), the PN junction reaches breakdown at approximately 16 V. Figure 4(b) shows that the transmission spectrum is

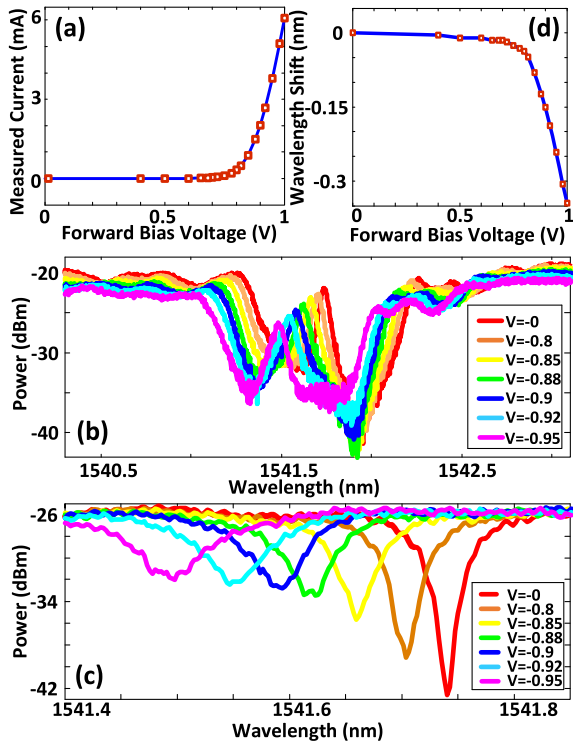


Fig. 3. (a) Measured V-I of the PN junction. (b) Wavelength shift of the transmission spectrum. (c) Notch wavelength shift when the PN junction is forward biased. (d) Wavelength shift when the bias voltage is increased.

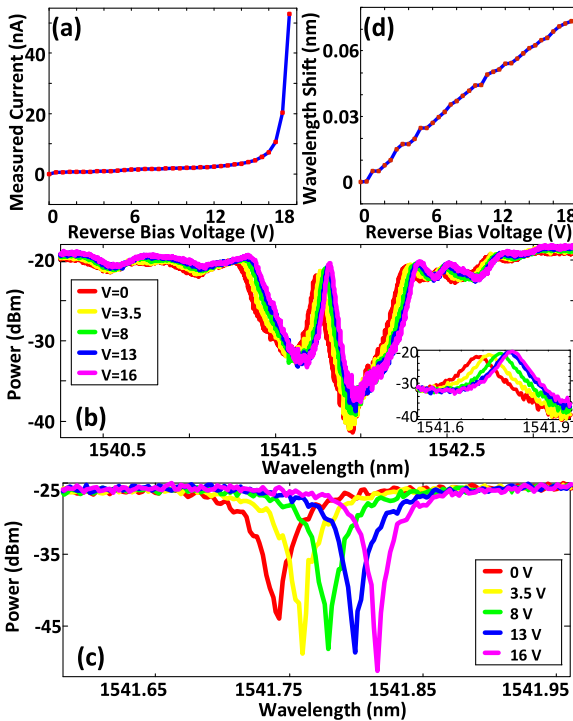


Fig. 4. (a) Measured V-I of the PN junction. (b) Wavelength shift of the transmission spectrum (inset: zoom-in view of the wavelength shift of the transmission window). (c) Notch wavelength shift when the PN junction is reverse biased. (d) Wavelength shift when the bias voltage is increasing.

red-shifted when the bias voltage is increased. When reverse biased, if the voltage is increased, more carriers are extracted and the depletion region is widened. Thus, an increased effective refractive index would lead to a red-shifted spectrum. Figure 4(c) shows the wavelength shift of the notch in reflection. When the bias voltage is increasing, the Q-factor is increasing due to the reduction in the free-carrier induced absorption loss. Meanwhile, the extinction ratio is also changed due to the change of the coupling condition [13]. For an injection current of 53 nA when biased at 17.5 V, the Q-factor is increased to 44,000, and the extinction ratio is increased to 25 dB. The notch wavelength is red-shifted by 73.6 pm. The tuning of the spectral response is shown in Fig. 4(d). The wavelength shift rate is estimated to be 4.2 pm/V.

The light-confining resonating structure of the FP cavity can enhance the effect of refractive index change, thus the TBG-FPF can be employed as an electro-optic modulator [14]. Similar to a silicon microring modulator [15], its 3-dB modulation bandwidth is determined by the RC time of the reverse-biased PN junction and the photon lifetime of the cavity. The photon lifetime is related to the Q-factor of the cavity given by $\tau = \lambda Q / 2\pi c$, where c is the speed of light in vacuum. The value of the Q-factor indicates the light-confinement capability of the cavity. To evaluate the performance of the filter as an electro-optic modulator, the frequency response of the TBG-FPF is first measured for a given input optical wavelength. Figures 5(a) and 5(b) show the transmission window of the TBG-FPF when a reverse-bias voltage of 3.5 and 8.0 V is applied, respectively, and three circles are used to indicate the different input wavelengths. Based on the estimated Q-factor, the photon-lifetime-determined cutoff frequency is calculated to be 6.3 GHz based on $f_r = 1/2\pi\tau$. Figure 5(c) shows the electro-optic frequency response for the three different input wavelengths. As can be seen, the maximum 3-dB modulation bandwidth is 5.6 GHz, which matches quite well with the calculated 3-dB bandwidth of 6.3 GHz. In addition, as can be observed, when the input wavelength is located at the peak of the transmission window, the frequency response, indicated in blue, has a 3-dB bandwidth of 1.5 GHz. When the

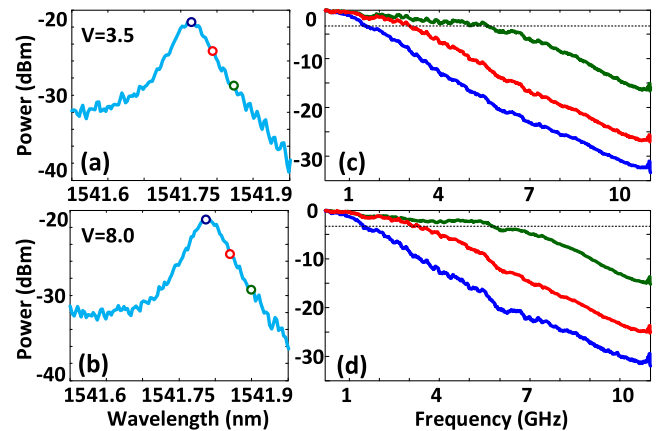


Fig. 5. Measured transmission window of the TBG-FPF when reverse biased with a voltage of (a) 3.5 V and (b) 8.0 V. (c) Measured frequency responses for three different wavelengths when the reverse bias voltage is 3.5 V, and (d) when the reverse bias voltage is 8.0 V.

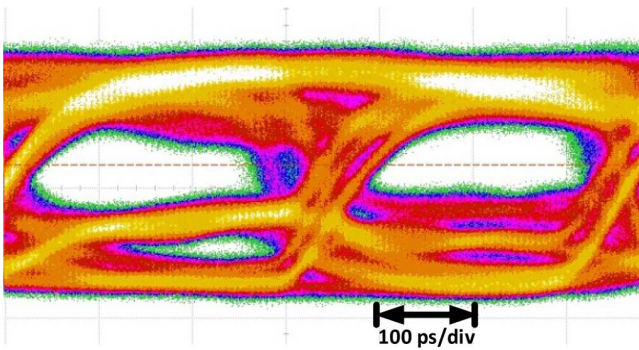


Fig. 6. Measured eye diagram for a nonreturn-to-zero pseudorandom binary sequence $2^7 - 1$ at 3.5 Gb/s.

input wavelength is away from the peak of the transmission window, the 3-dB bandwidth is increased to 3.1 GHz, as indicated in red in Fig. 5(c). When the input wavelength is farther away from the peak of the transmission window, the 3-dB bandwidth is further increased to 5.6 GHz, as indicated in green. As the wavelength of the input light is away from the resonance wavelength, the corresponding confinement capability of the cavity for that wavelength is becoming weaker, and its corresponding photon lifetime is becoming shorter. Therefore, the measured 3-dB modulation bandwidth is becoming larger. This photon-lifetime-dependent frequency response confirms that the modulation bandwidth of this TBG-FPF is mainly limited by the photon lifetime of the cavity. The same tendency of the electro-optic frequency response is found in Fig. 5(d), which shows the frequency response when the PN junction is reverse biased at 8.0 V.

The performance of using the TBG-FPF as a modulator to achieve high-speed modulation is also evaluated. In the experiment, the TBG-FPF is driven by a 3.5 Gb/s $2^7 - 1$ nonreturn-to-zero pseudorandom binary sequence with a V_{pp} of 1.8 V, generated by a pattern generator (Agilent N4901B). Eye diagram of the recovered electrical signal after photodetection is captured by a real-time oscilloscope (Infiniium 93204A), which is shown in Fig. 6. The eye diagram is quite open, which confirms that the TBG-FPF can be employed as a high-speed electro-optic modulator. Compared with a microring-based modulator, this filter has a higher fabrication tolerance and does not need a deliberately designed coupler. The performance of the filter as a modulator can also be further improved by optimizing the design of the FP cavity, the grating structure design, and the PN junction design.

In conclusion, we have designed, fabricated and tested a silicon-based on-chip electrically TBG-FPF. Spectral measurement showed the linewidth of the notch in the reflection band was approximately 46 pm with a Q-factor of 33,500 and an

extinction ratio was 16.4 dB. From the DC measurements, the average central wavelength shift rates in forward and reverse bias were -1.15 nm/V and 4.2 pm/V, respectively. The AC performance of the TBG-FPF was also evaluated. The electro-optic frequency response showed that the TBG-FPF had a 3-dB modulation bandwidth of ~ 5.6 GHz. The key feature of this design is that the filter has a high fabrication tolerance due to the incorporation of a PN junction to allow electronic tuning. The proposed TBG-FPF can find applications in optical sensing, narrowband tunable filtering, photonic processing of microwave signals, and high-speed electro-optic modulation.

Funding. Natural Sciences and Engineering Research Council of Canada (Conseil de Recherches en Sciences Naturelles et en Génie du Canada).

Acknowledgment. We acknowledge CMC Microsystems, for providing the design tools and enabling the fabrication of the device.

REFERENCES

1. H.-C. Kim, K. Ikeda, and Y. Fainman, *Opt. Lett.* **32**, 539 (2007).
2. Y. Painchaud, M. Aubé, G. Brochu, and M. Picard, *Bragg Gratings, Photosensitivity, and Poling in Glass Waveguides*, OSA Technical Digest (Optical Society of America, 2010), paper BTuC3.
3. G. P. Agrawal and S. Radic, *IEEE Photon. Technol. Lett.* **6**, 995 (1994).
4. F. Kong, W. Li, and J. P. Yao, *Opt. Lett.* **38**, 2611 (2013).
5. N. K. Berger, B. Levit, B. Fischer, M. Kulishov, D. V. Plant, and J. Azaña, *Opt. Express* **15**, 371 (2007).
6. A. W. Fang, E. Lively, Y. H. Kuo, D. Liang, and J. E. Bowers, *Opt. Express* **16**, 4413 (2008).
7. J. Sun, Purnawirman, E. S. Hosseini, J. D. B. Bradley, T. N. Adam, G. Leake, D. Coolbaugh, and M. R. Watts, *Opt. Lett.* **38**, 4002 (2013).
8. X. Zou, M. Li, L. Yan, J. Azana, and J. P. Yao, *Opt. Lett.* **38**, 3096 (2013).
9. R. A. Soref and B. R. Bennett, *IEEE J. Quantum Electron.* **23**, 123 (1987).
10. Y. Wang, J. Flueckiger, C. Lin, and L. Chrostowski, *Proc. SPIE* **8915**, 89150Y (2013).
11. Y. Zhang, S. Yang, A. E.-J. Lim, G.-Q. Lo, C. Galland, T. Baehr-Jones, and M. Hochberg, *Opt. Express* **21**, 1310 (2013).
12. A. D. Simard, N. Belhadj, Y. Painchaud, and S. LaRochelle, *IEEE Photon. Technol. Lett.* **24**, 1033 (2012).
13. W. Shi, X. Wang, C. Lin, H. Yun, Y. Liu, T. Baehr-Jones, M. Hochberg, N. A. F. Jaeger, and L. Chrostowski, *Opt. Express* **21**, 3633 (2013).
14. Q. Xu, B. Schmidt, S. Pradhan, and M. Lipson, *Nature* **435**, 325 (2005).
15. P. Dong, S. Liao, D. Feng, H. Liang, D. Zheng, R. Shafiqi, C.-C. Kung, W. Qian, G. Li, X. Zheng, A. V. Krishnamoorthy, and M. Asghari, *Opt. Express* **17**, 22484 (2009).